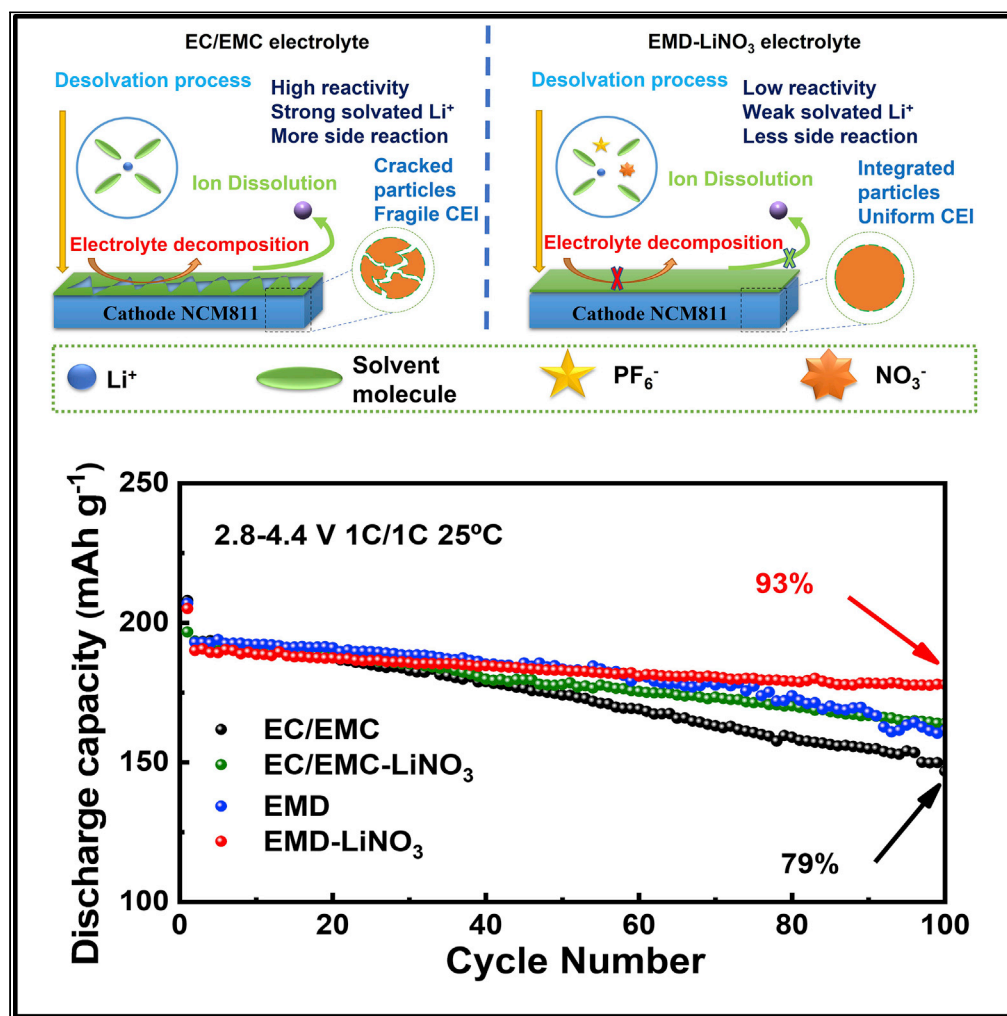**Article**

Weakly solvated EC-free linear alkyl carbonate electrolytes for Ni-rich cathode in rechargeable lithium battery

Guohuang Kang,
Geng Zhong,
Jiabin Ma, ..., Zhen
Chen, Feiyu Kang,
Yidan Cao

fykang@sz.tsinghua.edu.cn
(F.K.)
yidancao@sz.tsinghua.edu.cn
(Y.C.)

Highlights

Ethylene carbonate (EC)-
free linear alkyl carbonate-
based electrolyte is
developed

The EC-free electrolyte
possesses low viscosity
and weakly solvated
structure

Li_3N-LiF-enriched SEI and
robust CEI are formed to
elevate cycle stability

High-voltage ($\geq 4.4V$) and
low-temperature ($-30°C$)
performance of NCM811
is improved

Article

Weakly solvated EC-free linear alkyl carbonate electrolytes for Ni-rich cathode in rechargeable lithium battery

Guohuang Kang,[1,2] Geng Zhong,[1,2] Jiabin Ma,[1,2] Rui Yin,[1] Kangning Cai,[1,2] Tianqi Jia,[1,2] Xiaolong Ren,[1] Kuang Yu,[1,2] Peiwu Qin,[2,3] Zhen Chen,[1] Feiyu Kang,[1,2,*] and Yidan Cao[1,2,4,*]

SUMMARY

Ethylene carbonate (EC) in the electrolyte is not stable in cells operated at high voltage ($\geq 4.4V$) or with Li metal anode, which greatly reduce the energy density and lifetime of the rechargeable lithium battery. Herein, an EC-free linear alkyl carbonate-based electrolyte is developed, which enables the high-voltage ($\geq 4.4V$) and low-temperature ($-30°C$) application of Ni-rich cathode ($LiNi_{0.8}Mn_{0.1}Co_{0.1}O_2$, NCM811). The EC-free system, consisting of $LiPF_6$ and $LiNO_3$ in ternary linear alkyl carbonates, possesses low viscosity, weakly solvated structure, and high interfacial stability with both the Ni-rich cathode and the Li metal anode to avoid continuous electrode/electrolyte side reactions and metal dissolution from the cathode. As a result, the Li‖NCM811 cell delivers remarkable capacity retention of $93 \pm 0.5\%$ at the voltage of 4.4V and $88 \pm 0.6\%$ at 4.5V over 100 cycles. This study provides very encouraging perspective to develop EC-free carbonate-based electrolyte for high-voltage and low-temperature application in high-energy-density rechargeable lithium batteries.

INTRODUCTION

The lithium-ion batteries (LIBs) have received great success as rechargeable batteries for portable electronic devices and extended their application to electric vehicles and stationary renewable energy storage, which attracts intense research efforts to further improve the energy density of batteries considering that the conventional lithium-ion battery is approaching its energy-density limit.[1–5] Rechargeable battery consisting of lithium metal anode, which possesses extremely high specific capacity (3862mAh/g) and ultralow electrochemical redox potential ($-3.04V$ versus the standard hydrogen electrode), and high-capacity, high-voltage cathode is considered as one of the most promising alternative battery systems to maximize the energy density.[6] Continuous attempts have been taken to further increase the energy density by developing cathode materials those can operate above 4.4 V versus Li/Li$^+$, such as $LiNi_xMn_{2-x}O_4$,[6] $LiCoPO_4$.[7] Nickel (Ni)-rich $LiNi_xMn_yCo_{1-x-y}O_2$ (NMC) cathode materials with less Co contents, like $LiNi_{0.8}Mn_{0.1}Co_{0.1}O_2$ (NMC811),[8,9] have attracted significant attention because of their high capacity and low cost. However, the development of high-voltage batteries is confronted with tremendous challenges because of the high reactivity of electrolytes with both the high-voltage cathode and lithium metal anode.

Currently, the state-of-the-art commercial electrolytes are based on mixtures containing $LiPF_6$, ethylene carbonate (EC), and linear carbonates like ethyl methyl carbonate (EMC), dimethyl carbonate (DMC) and diethyl carbonate (DEC). However, the EC-based electrolytes are not appropriate for operation above 4.3 V because of the high anodic reactivity of EC.[10] EC in the electrolyte may be continuously oxidized at the positive electrode in cells operated at high voltage and lead to lithium salt consumption, gas generation and impedance growth at the cathode/electrolyte interface,[10] which would greatly reduce the energy density and the lifetime of the battery.[11–13] Various methods, including electrolyte additives and new electrolyte solvents, have been utilized to expand the electrochemical window of the electrolyte and enable the high-voltage stability of the batteries, especially for the Ni-rich cathode.[8,14–19] Han et al.[14] found that the succinonitrile additive effectively induces stable and efficient cathode/electrolyte interphase, which significantly improves the high-voltage (4.4V) cycle performance of NCM523/graphite battery. Dual functional electrolyte additives, which can facilitate stable interfacial layer at both anode and cathode sides, have also been investigated. Duan[15] et al. used lithium difluorophosphate ($LiPO_2F_2$) with low LUMO

[1]Institute of Materials Research, Shenzhen International Graduate School, Tsinghua University, Shenzhen, China

[2]Tsinghua-Berkeley Shenzhen Institute, Shenzhen International Graduate School, Tsinghua University, Shenzhen, China

[3]Institute of Biopharmaceutical and Health Engineering, Shenzhen International Graduate School, Tsinghua University, Shenzhen, China

[4]Lead contact

*Correspondence:
fykang@sz.tsinghua.edu.cn (F.K.),
yidancao@sz.tsinghua.edu.cn (Y.C.)

https://doi.org/10.1016/j.isci.2022.105710

energy and organic 1,3,6-hexanetrinitrile (HTN) with low HOMO energy as synergistic inorganic-organic dual-functional additives in the carbonate electrolyte to achieve practical high-voltage (4.7V) lithium-ion batteries. Xia et al.[16,17] investigated on several additives, including succinic anhydride, prop-1-ene,1,3-sultone (PES), methylene methanedisulfonate (MMDS), propanediol cyclic sulfate (trimethylene sulfate-TMS), as enabler in ethylene carbonate-free linear alkyl carbonate electrolyte for high voltage Li-ion cells. Ming's group[18,19] tuned the lithium solvation structure and invented an interfacial model to reveal the working mechanism of the high-voltage electrolytes, which incorporating molecular-scale interactions between the lithium-ion, anion, and solvents at the electrolyte–electrode interfaces to help interpret battery performance. Besides the investigation on additives for EC-based electrolytes to suppress the detrimental parasitic reactions with cathodes at high voltage, development of EC-free solvents, such as ionic liquids,[20] alkyl dinitrile compounds,[21] alkyl sulfones[22] or fluorinated alkyl carbonates,[23] is also attractive and promising because of their good compatibility with high-voltage cathodes. However, the low compatibility with anode and the high cost of these solvents limits their practical application. To improve the compatibility between the electrolyte and electrodes, Xue et al.[24] developed "full fluorosulfonyl" electrolyte with "FSI-inspired solvent'' dimethylsulfamoyl fluoride ($FSO_2NC_2H_6$) to get the highly compatible electrolyte with both Li metal anode and metal-oxide cathode. They also reported sulfonamide-based electrolyte to not only suppress side reactions, stress-corrosion cracking, transition-metal dissolution and impedance growth on the cathode side but also enable highly reversible Li metal plating and stripping.[25] Yu et al.[26,27] found that partially fluorinated, locally polar –CHF_2 is the optimal group in a family of fluorinated-1,2-diethoxyethanes as electrolyte solvents, rather than fully fluorinated –CF_3 in common designs, leading to excellent compatibility with both Li metal anode and high-voltage cathode. However, the high cost and difficulty in synthesis still limit the practical use of these solvents/additives. High-voltage electrolytes with low-cost are still highly desired.

Here, in this work, we propose an EC-free low-cost linear alkyl carbonate-based electrolyte and realize the high-voltage application in rechargeable lithium battery. The EC-free system, consisting of ternary linear alkyl carbonates (EMC + DMC + DEC), enables excellent electrochemical performance at high-voltage (≥4.4V) as well as low-temperature (−30°C) because of its low viscosity, weakly solvated structure and high interfacial stability with both the positive and negative electrodes. Additional introduction of lithium nitrate additives further enhances the performance of the electrolyte and facilitates stable SEI to synergistically improve the electrochemical performance of the Ni-rich cathode in high-energy-density battery. This work provides a very encouraging design strategy of EC-free electrolyte, and highlights the potential of ester-based electrolyte for high-voltage applications in high-energy-density rechargeable lithium batteries.

RESULTS

Properties of the EC-free electrolyte

1M $LiPF_6$ was dissolved in ethyl methyl carbonate (EMC), dimethyl carbonate (DMC) and diethyl carbonate (DEC) (volume ratio 1:1:1) with 2 vol.% fluoroethylene carbonate (FEC) to get the linear alkyl carbonate-based electrolyte (denoted by EMD). FEC is a commonly used additive to stabilize the solid electrolyte interphase layer on the electrode.[28] 1 wt.% lithium nitrate ($LiNO_3$) was added in the EMD electrolyte to get the further modified electrolyte (denoted by EMD-$LiNO_3$). Commercial electrolyte consisting of 1M $LiPF_6$ in ethylene carbonate (EC) and ethyl methyl carbonate (EMC) (volume ratio 3:7) with 2 vol.% fluoroethylene carbonate (FEC) (denoted by EC/EMC) was used as a reference.

Figure 1A shows the molecular structure of the carbonate solvents, including the cyclic structured EC and the rest linear carbonates. FTIR absorption spectra of the electrolytes are shown in Figure S1. The peaks located around 1740 cm^{-1} are attributed to the stretching vibration of carbonyl C=O groups in the solvents,[29] whereas new peaks (splitting peaks) around 1800 cm^{-1} in the EC/EMC electrolyte may be because of the strong solvated Li$^+$ in EC.[30] Compared with EC/EMC sample, the EMD-based electrolyte shows weakened coordination between lithium ions and the solvents. Previous investigations showed that Li$^+$ preferentially interacts with the carbonyl oxygen atom in carbonate molecules (Li$^+$···O=C).[31] The peaks at ~1258 cm^{-1}, 1135 cm^{-1} are attributed to the stretching vibration of ethereal O-C-O groups in solvated Li$^+$ clusters,[29] and extra strong peaks at wave numbers of ~1160 cm^{-1}, 1070 cm^{-1} in EC/EMC are related to the formation of solvated Li$^+$···EC.[32]

The P-F stretching vibrations appear in the range of 810-900 cm^{-1}, as shown in Figure 1B. Signals around 875 cm^{-1} are ascribed to the PF$_6^-$ ions coordinated with Li$^+$, and more Li$^+$-PF$_6^-$ ion pairs show up in the
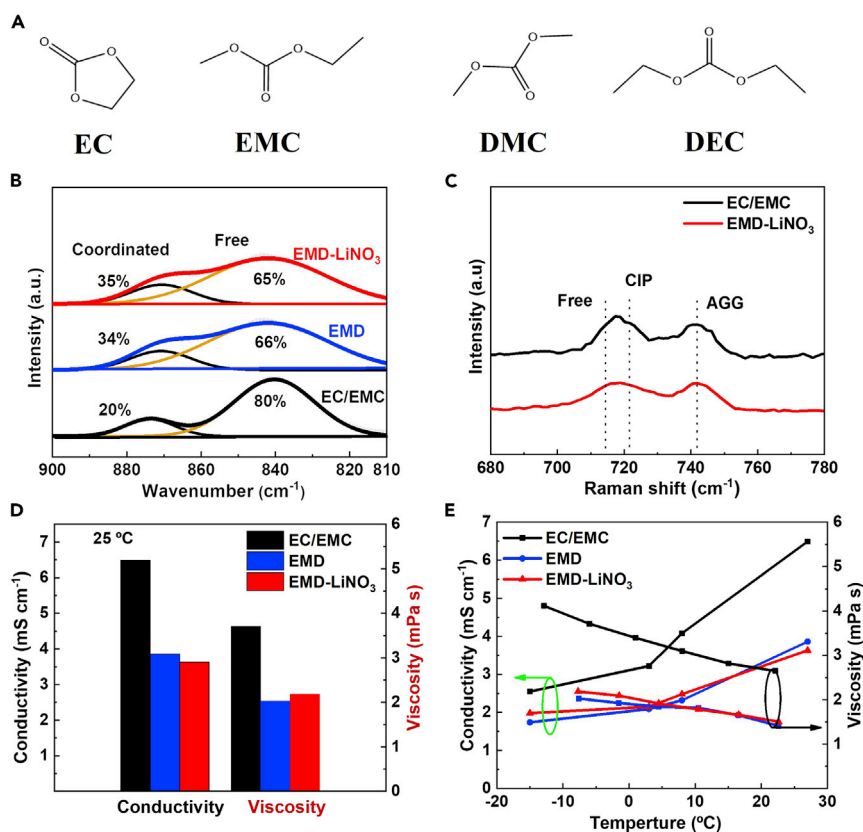
Figure 1. The molecular structure and physical properties of electrolytes

(A) Molecular structure of ethylene carbonate (EC), ethyl methyl carbonate (EMC), dimethyl carbonate (DMC), and diethyl carbonate (DEC).

(B) FTIR spectra of the P-F vibrations in EC/EMC, EMD and EMD-LiNO$_3$.

(C) Raman spectra of EC/EMC and EMD-LiNO$_3$.

(D) Ionic conductivity and viscosity of EC/EMC, EMD and EMD-LiNO$_3$.

(E) Ionic conductivity and viscosity of EC/EMC, EMD and EMD-LiNO$_3$ electrolytes at different temperatures.

EMD and EMD-LiNO$_3$ solutions ($\sim$34–35%) compared with the EC/EMC electrolyte ($\sim$20%), indicating more contact ion pairs (CIP, i.e. one PF$_6^-$ anion interacting with one Li$^+$) and aggregates (AGG, i.e., one PF$_6^-$ anion interacting with two or more Li$^+$) in the EMD-based electrolytes.[33] CIPs and AGGs structures would arise when the electrostatic interaction between anions and cations are stronger than that between cations and solvent molecules. CIP and AGGs structures can be generated by weakening the solvability of solvents. These complexes are thermodynamically more stable than free solvent molecules, and can provide wider operating temperature and voltage windows.[34,35] The more PF$_6^-$ anions into the solvated sheath of Li$^+$ in the EMD suggests the weak solvation of Li$^+$ with the solvents, which would be beneficial to improve the electrochemical stability of the electrolyte.[36] The peaks around 840 cm^{-1} corresponding to free PF$_6^-$ anions show reduced contribution in the EMD-based electrolyte compared with the EC/EMC, indicating less free uncoordinated PF$_6^-$ and more free solvents, which reveals that Li$^+$ ions are relatively weak solvated with the solvents in the EMD-based solution.[36]

The Raman bands (Figure 1C) at 700–780 cm^{-1} arise from the vibration of PF$_6^-$ anions. The bands at 715 cm^{-1}, 722 cm^{-1}, and 742 cm^{-1} are attributed to free PF$_6^-$ anion, contact-ion pairs, and aggregates, respectively.[37–39] The proportion of free PF$_6^-$ anion is higher in the EC/EMC electrolyte, because of the strong Li$^+$ coordinating ability of EC solvent, compared with that in the EC-free electrolyte. By contrast, the contents of CIPs and AGGs are higher in the EMD-LiNO$_3$ electrolyte. It suggests that lithium ions and solvent molecules in the EMD-based electrolyte form a weakly solvated structure, and PF$_6^-$ anions are involved in the solvation, which is consistent with the above FTIR results.
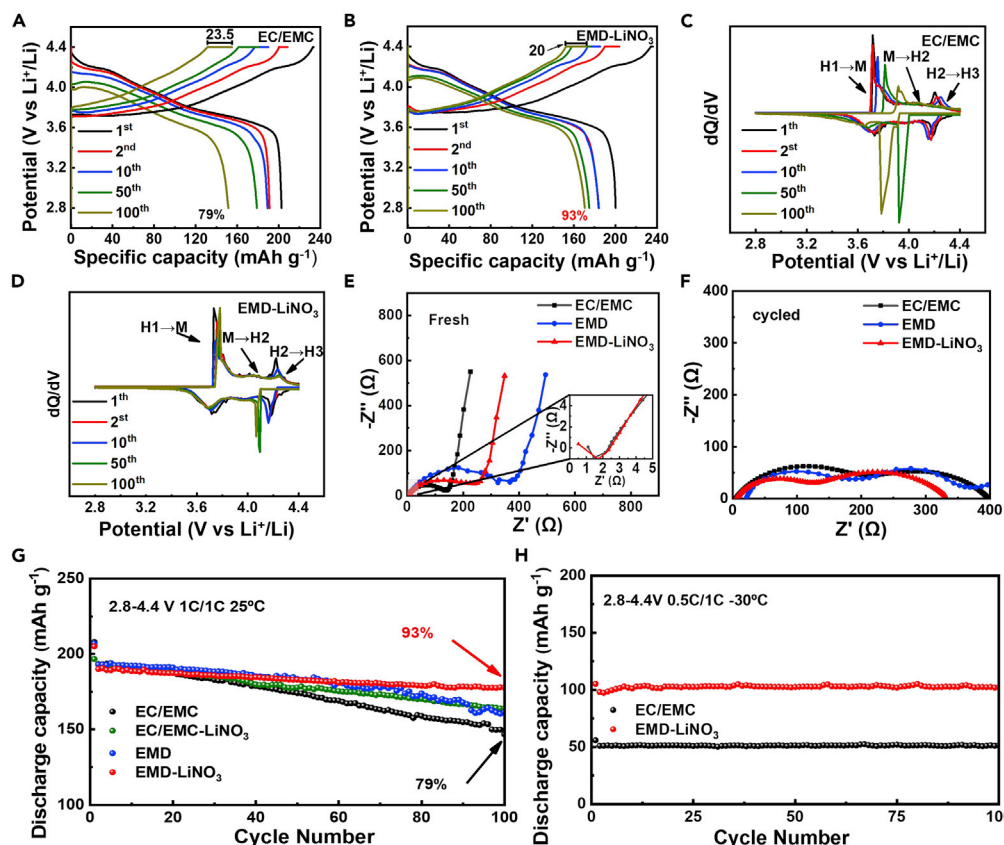
Figure 2. Electrochemical performance of Li||NCM811 half cells

(A and B) Voltage curves of cells with EC/EMC (A) and EMD-LiNO$_3$ (B) electrolytes cycled in 2.8–4.4V at 25°C.

(C and D) Differential capacity curves of cells with EC/EMC (C) and EMD-LiNO$_3$ (D) electrolytes cycled at 2.8–4.4V.

(E and F) Electrochemical impedance spectroscopy of cells with EC/EMC and EMD-LiNO$_3$ before (E) and after 50 cycles (F).

(G) Cycling performances of cells cycled in 2.8–4.4V at 25°C.

(H) Cycling performances of cells cycled in 2.8–4.4V at −30°C.

Figure 1D shows that compared with the EC/EMC electrolyte, the conductivity of the EMD and EMD-LiNO$_3$ is reduced, which is because of the relatively lower dielectric constant of linear alkyl carbonates compared to the cyclic EC. However, the viscosity of the EMD and EMD-LiNO$_3$ electrolyte is about half lower than that of the EC/EMC electrolyte, which may provide promising potential for low-temperature application. The dependence of conductivity and viscosity on temperature (Figure 1E) demonstrates that the EMD based electrolytes possess much lower viscosity of <2 mPa·s in a wide temperature window and the ionic conductivity of the EC/EMC electrolyte drops quickly with decreasing temperature, whereas the EMD based electrolytes are more tolerant to low temperatures. Figure S2 shows that the electrochemical window of the mixed EMD-based electrolytes is ≥ 4.4 V, which is applicable to most commonly used cathode materials. In addition, this solvent replacement save on cost of the electrolyte. As calculated based on the prices of the solvents (Tables S1), the cost of the electrolyte can be deducted by 37% by using EC-free linear alkyl carbonate solvents.

Electrochemical performance of Li||NCM811 cells

The voltage profiles and differential capacity plots of NCM811/Li cells with EC/EMC and EMD-LiNO$_3$ electrolytes are representatively compared in Figures 2A–2D. Figures 2A and 2B show the voltage curves over the first, 10th, 50th and 100th cycles. In the first cycle, cathodes in the EC/EMC and EMD-LiNO$_3$ both show typical phase transition (H1 ⇆ H2 ⇆ H3) behavior of the NCM811 cathode.[40] The voltage profiles show faster capacity decay in the EC/EMC electrolyte, especially at ~4.2V related to the H2→H3 phase

transition. Such great fade could be related to the instable lattice structure of the cathode and the increase of cell impedance, which may be caused by the unstable CEI, structural degradation and transition metal dissolution from the cathode.[41] The capacity retention of cell in the EC/EMC electrolyte is 79 ± 0.7% after 100 cycles. In contrast, the cell cycled in the EMD-LiNO$_3$ electrolyte is much more stable, maintaining capacity retention of 93 ± 0.5%. Besides, there are also obvious differences of the restored capacity during the trickle charge, i.e., constant voltage (4.4V), process. The restored capacity increases with electrode polarization. Figure 2A shows that the capacity change during trickle is 23.5mAh g^{-1} after 100 cycles. However, Figure 2B shows that the platform during trickle charge corresponds to only 20 mAh g^{-1} after 100 cycles in the EMD-LiNO$_3$ electrolyte, indicating reduced polarization. It demonstrates that the EMD-LiNO$_3$ electrolyte can effectively alleviate the increase of electrode polarization.

Figures 2C and 2D depict the differential capacity curves of cells in the EC/EMC and EMD-LiNO$_3$ electrolytes. Three main redox peaks during cycling are because of the hexagonal (H1) ⇆ monoclinic(M) ⇆hexagonal(H2) ⇆hexagonal(H3) phase transitions of the NCM811 cathode.[42] More obvious shifts of the phase transition peaks are observed in the EC/EMC electrolyte, indicating faster cathode degradation. The charge/discharge polarization also increases during cycling, and the EC/EMC cell shows higher polarization, especially for the H2 ⇆H3 phase transition. The redox peaks around 4.2 V, corresponding to the H2→H3 phase transition, is known to be responsible for fast capacity fading. This phase transition tends to cause a sudden contraction of the NCM cell in the c-direction, resulting in large micro-strain and subsequently deteriorating the rechargeability. The H2→H3 transition peak totally distorted after 50 cycles in the cell with EC/EMC electrolyte, whereas it is relatively better preserved in the EMD-LiNO$_3$ electrolyte even after 100 cycles. The shift and distortion of the redox peaks are caused by the deteriorating reversibility of the cathode, and the results indicate that the reversibility and structural integrity of the cathode are effectively improved in the EMD-LiNO$_3$ electrolyte.

The resistance of cells during cycling was characterized by electrochemical impedance spectroscopy (EIS) to further understand the evolution of cathodes during cycling. Figures 2E and 2F show the Nyquist plots of the uncycled and cycled cells. For the fresh cells, the bulk resistance of the cell (Rs) are similar for both electrolytes (1.45 Ω-EC/EMC and 1.7 Ω- EMD-LiNO$_3$, respectively).[43] The EMD-LiNO$_3$ sample shows higher charge transfer resistance (R$_{ct}$, high-frequency semicircle) initially, which may be related to the relatively low ionic conductivity of the linear alkyl carbonates as shown in Figures 1D and 1E. After cycling, cathode electrolyte interphase (CEI) is formed on the surface of the positive electrode, resulting in an extra semicircular in the high frequency region (R$_f$) (Figures S3 and 2F).[44] The internal resistance of the cells does not change after cycling. After 50 cycles, the CEI resistance is 125 Ω in the EMD-LiNO$_3$, which is way lower than that in the EC/EMC (212 Ω) and EMD (350Ω), indicating that the CEI layer is more conductive in the EMD-LiNO$_3$ electrolyte. The R$_{ct}$ is increased from 125 Ω to 195 Ω in the EC/EMC electrolyte, but it is decreased from 350 Ω to 191 Ω in the EMD electrolyte and from 240 Ω to 190 Ω in the EMD-LiNO$_3$ electrolyte, respectively, indicating the EMD-based electrolyte can effectively facilitate the interfacial charge transfer behavior during cycling.

Figures 2G and 2H show the cycling performance of the cells with EC/EMC and EMD-LiNO$_3$ electrolyte. Upon cycling at 1C and 2.8–4.4V, the cell with EMD-LiNO$_3$ electrolyte show remarkable capacity retention of 93 ± 0.5% after 100 cycles, way higher than those of the EMD cell, EC/EMC-LiNO$_3$ (EC/EMC+1 wt.% LiNO$_3$) cell, and the EC/EMC cell. A series of electrolytes with different compositions were tested at the same condition (Figure S4A), and it turns out that the EMD, i.e., EMC/DMC/DEC = 1/1/1 (vol.), is the most favorable composition. In addition, the EMD-LiNO$_3$ cell retains 87 ± 0.4% of its initial capacity after 150 cycles at 0°C, much higher than 75 ± 1% of the EC/EMC cell (Figure S8), suggesting a much better low-temperature performance, which could be attributed to the less reduced conductivity of the EMD-based electrolyte at low temperatures as shown in Figure 1E. Figure S4B verifies the adaptability of the EMD-based electrolyte at higher cut-off voltage of 4.5V. The EMD-LiNO$_3$ cell achieves remarkable capacity retention of 88 ± 0.6% after 100 cycles, which is much higher than that of 59 ± 0.5% in the traditional EC-based electrolyte. Figures S5 and S6 further demonstrate the applicability of the EMD-LiNO$_3$ electrolyte in the anode-free Li||Cu cell (Figure S5A), Li||Li symmetric cell (Figure S5B) and graphite||NCM811 full cell (Figure S6). Compared to the baseline, the EMD-LiNO$_3$ cells excel with much higher capacity retention. The rate-performance is also improved to some extent by the EMD-LiNO$_3$ electrolyte (Figure S7), which may be related to the lower interfacial resistance and faster charge transfer at the cathode/electrolyte interface as revealed above. In addition, the EMD-LiNO$_3$ cell exhibits much superior cyclability even under low
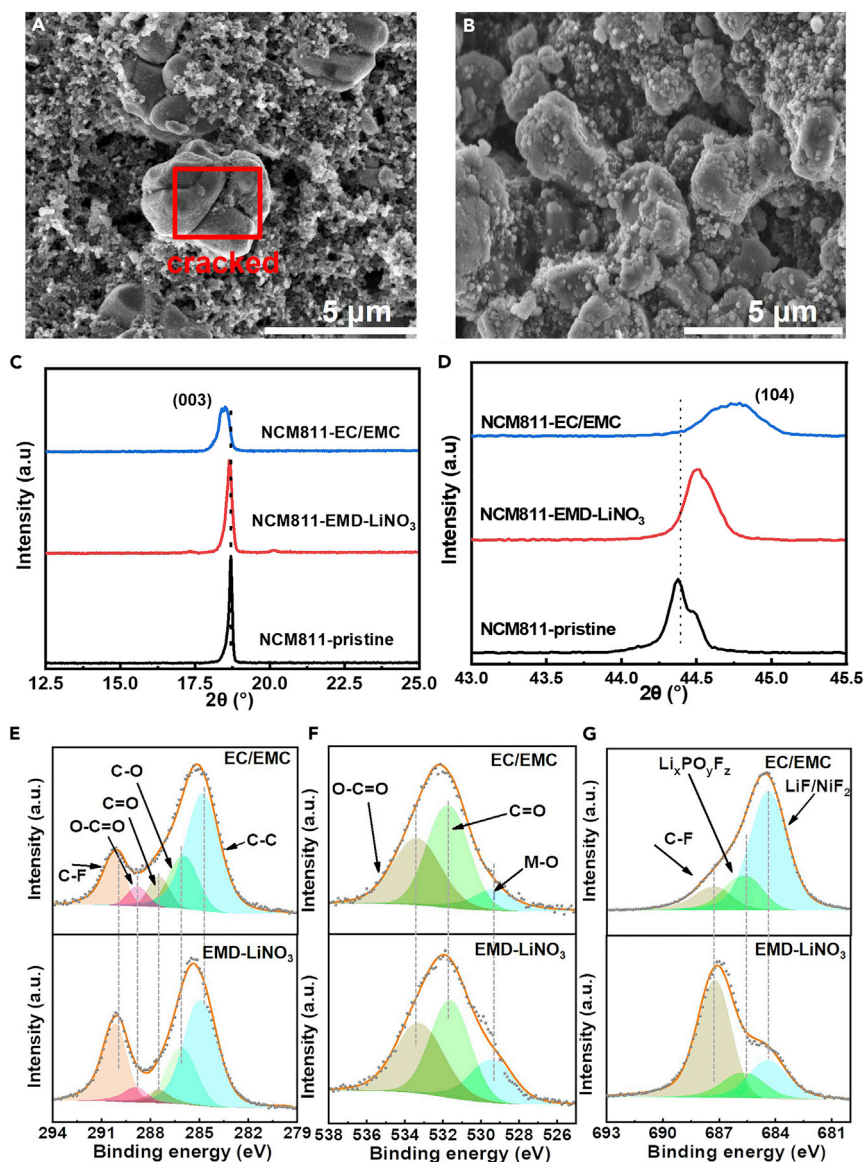
Figure 3. Morphology and structural characterization of cathode

(A and B) SEM images of the NCM811 cathodes cycled in the EC/EMC (A) and EMD-LINO$_3$ (B) electrolytes.

(C and D) The XRD pattern of NCM811 cathode materials before (black line) and after 50 cycles in the EC/EMC (blue line) and EMD-LiNO$_3$ (red line) electrolytes.

(E–G) XPS spectra of C1s (E), O1s (F) and F1s (G) of NCM811 cathode cycled in EC/EMC and EMD-LiNO$_3$ electrolyte.

temperature of −30°C (Figure 2H) and the delivered capacity of NCM811 is improved by twice compared to the EC/EMC cell, further demonstrating the applicability of the developed electrolyte.

Cathode/electrolyte interface

The surface morphology and microstructure of the cycled cathodes were characterized to understand the effects of electrolytes on the cathode/electrolyte interface. The cathode particles are integrated and uniform with an average particle size of ∼2 μm before cycling (Figure S9). Cracks show up in the cathode particles after cycling in the EC/EMC electrolyte (Figure 3A), whereas the cycled cathode particles in the EMD-LiNO$_3$ electrolyte are more integrated without obvious particle fracture (Figure 3B). It demonstrates that the structural evolution of the NCM811 cathode during cycling is dependent on the electrolyte and dramatic structural changes during cycling is significantly suppressed in the EMD-LiNO$_3$ electrolyte.

The microstructure of the pristine and cycled cathodes was further characterized by XRD (Figures S10, 3C, and 3D). As shown in Figure S10, the main diffraction peaks in the samples belong to the α-NaFeO$_2$ structure (R3m). Obvious peak splittings located at 37.5–39.0° (006)/(102) and 64.0–65.5°(108)/(110) confirm the high crystallinity and well-formed layered structure of the cathodes.[40] After cycling, the peak structures mentioned above are well maintained in the EMD-LiNO$_3$ electrolyte. However, the peaks shift and the characterized peak splittings of the cathode diminish after cycling in the EC/EMC electrolyte, indicating the layered structure of the cathode may be partially destroyed.

There are obvious peak shifts around ~17.5–20.0° ((003) peaks), ~35.0–40.0° ((101) peaks), and 44.0–45.0° ((104) peaks), etc. after cycling, especially for the cycled cathode in the EC/EMC electrolyte. As shown in Figure 3C, the (003) peak shifts to lower 2θ angles with peak broadening after cycling in the EC/EMC, indicating reduced crystallinity and an enlargement of lattice along the c-axes. C-axes expansion suggests that parts of the particles may exist in the H2 phase, is caused by the irreversible phase transition during cycling, suggesting inferior reversibility of the cathode in the EC/EMC electrolyte. By contrast, the cathode cycled in the EMD-LiNO$_3$ electrolyte maintains its crystalline structure without obvious peak shift and broadening, indicating that the reversibility of the NCM811 crystalline structure is greatly improved. More obvious peak shifts and broadening are observed for the (104) peaks in the cathode cycling in the EC/EMC, further confirming the improved reversibility of the cathode and the superiority of the EMD-LiNO$_3$ over the EC/EMC, which is consistent with the above results in Figures 2A–2D.

As a measure of the Li/Ni disorder in the layered NCM cathode materials,[9,45,46] it has been reported that the higher value of I (003)/I (104), the better layered structure. The intensity ratio of (003)/(104) peaks are 1.39, 1.33 and 1.23 for the pristine cathode, cycled cathodes in EC/EMC and EMD-LiNO$_3$ electrolytes, respectively. Compared with the pristine cathode (I(003)/I(104) = 1.39), the decrease of the I(003)/I(104) ratios for the cycled cathodes in the EC/EMC and EMD-LiNO$_3$ indicates that the cathodes suffer in different degrees of irreversible layered-spinel-rock salt phase transition, which could be related to the transition metal dissolution and the loss of oxygen.[11,13] Compared with the EC/EMC, the EMD-LiNO$_3$ electrolyte can effectively mitigate the intrinsic structural change and alleviate the severe lattice changes of the cathode during cycling. The cathode cycled in the EMD-LiNO$_3$ is more resistant to microcracking and the structural integrity and stability are greatly improved. As a result, the cycling degradation is efficiently suppressed in the EMD-LINO$_3$ electrolytes compared with the EC/EMC one.

X-ray photoelectron spectroscopy (XPS) analysis on the cycled cathodes was conducted to understand the composition of CEI and the interfacial changes between the cathode and the electrolyte during cycling. The C1s spectra (Figure 3E) consist of peaks corresponding to C-F (290.1 eV), O-C=O (288.8 eV), C=O (287.5 eV), C–O (286.1 eV) and C–C (284.7 eV).[42] The total contents of C-O=C, C=O species, which are closely related to the decomposition of electrolyte solvents and the formation of organic components in the CEI, are decreased in the EMD-LiNO$_3$ compared to the EC/EMC case. The increased amounts of C-F species, which is related to the PVDF binder in the cathode and the by-products of PF$_6^-$ decomposition, in the EMD-LiNO$_3$ case indicates thinner CEI on the surface and the participation of PF$_6^-$ in the CEI formation. The O 1s spectra (Figure 3F) include peaks corresponding to the M−O (529.3 eV), C=O (531.6 eV) and O-C=O(533.2 eV).[40] Compared with the cathode in the EC/EMC electrolyte, the cathode in the EMD-LiNO$_3$ electrolyte consists of decreased amount of C=O and O-C=O. The reduced amount of organic components in the CEI, indicating less side reactions between the cathode and the solvents, has been proved to be beneficial for the stability of the CEI layer.[42] Increased amount of M−O (metal-oxide) derived from the active NCM811 material is detected in the EMD-LiNO$_3$ case, indicating a much thinner and more uniform CEI layer is formed on the surface of the cathode in the EMD-LiNO$_3$ electrolyte.

There are three peaks corresponding to the C-F (687.2 eV), Li$_x$PO$_y$F$_z$ (685.6 eV), and LiF/NiF$_2$ (684.4 eV)[40] in the F 1s spectra of the cycled cathodes. The amount of LiF/NiF$_2$ species is reduced in the CEI layer formed in the EMD-LiNO$_3$ electrolyte. The highly resistive LiF/NiF$_2$ species on the surface are derived from the LiPF$_6$ decomposition products and hydrofluoric acid (HF) attack.[42] LiF/NiF$_2$ species have been reported to be detrimental to Li ion transport kinetics, resulting in capacity fade.[47] In addition, the acidic species could attack the surface of the layered cathode, facilitate dissolution of transition metals, and aggravate Li$^+$/Ni^{2+} cation mixing as well as disordered rock-salt phase formation owing to insufficient coordinating oxygen caused by the corrosion reactions. The substantially reduced LiF/NiF$_2$ species in the CEI layer by replacing EC/EMC with EMD-LiNO$_3$ electrolyte further demonstrates that the side reactions between Li$^+$
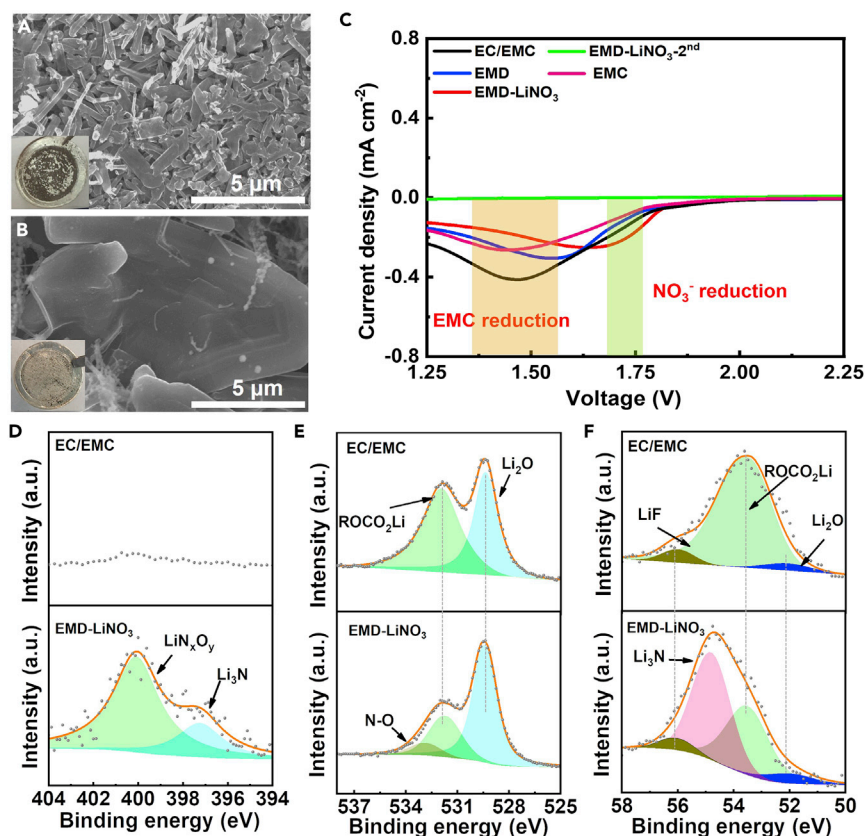
Figure 4. Morphology and structural characterization of anode

(A and B) SEM images of the deposited lithium anode in the EC/EMC (A) and (B) EMD-LINO$_3$ electrolyte.

(C) The CV curves of cells in EC/EMC, EMD, EMD-LiNO$_3$ and EMC electrolytes.

(D–F) The XPS spectra of N1s (D), O1s (E) and Li1s (F) of the anode cycled in EC/EMC and EMD-LiNO$_3$ electrolyte.

and electrolyte are significantly suppressed. Meanwhile, less Li$_x$PO$_y$F$_z$ because of electrolyte decomposition and more C-F species attributed to PVDF binder are detected in the EMD-LiNO$_3$ case, indicating a thinner CEI layer on the cathode in EMD-LiNO$_3$ electrolyte. The above results demonstrate that the continuous side reactions between the cathode and the electrolyte, and the dissolution of transition metal ions are effectively suppressed to avoid CEI/cathode fracture; as a result, thin and stable CEI is established on the surface of the NCM811 cathode even after prolonged cycling in the EMD-LiNO$_3$ electrolyte. The uniform cathode/electrolyte interfacial structure and improved stability of the CEI layer induced by the EMD-LiNO$_3$ electrolyte greatly reduce the interfacial impedance, as revealed in Figure 2G, and promote the cyclability of the NCM811 in the EMD-LiNO$_3$ electrolyte.

Anode/electrolyte interface

The morphology of the deposited Li in different carbonated electrolytes was studied by SEM. Deposits of lithium in the EC/EMC electrolyte exhibit porous dendrite-like structure (Figure 4A). Remarkably dense mosaic-shaped Li deposition with a size of ∼10 μm without obvious formation of dendrites are developed in the favor of the EMD-LiNO$_3$ electrolyte (Figure 4B). Compared with the porous and dark-colored surface in the EC/EMC, the surface of Li metal anode in the EMD-LiNO$_3$ electrolyte is dense and shiny without obvious defects (insets in Figures 4A and 4B). This distinct difference in appearance is mainly because of the improved uniformity and decreased porosity of Li deposition. The reduced porosity and surface area of the deposited Li film would be able to mitigate the continuous side reaction with the electrolyte and facilitate a robust SEI layer.[42] Figure 4C shows that two broad peaks show up during the initial reduction. The peak at ∼1.5V is mainly because of the reduction of EMC, which is consistent with the pure EMC electrolyte. The shift of the reduction peak in the EMD electrolyte may be caused by DMC (Figure S11, ∼1.85V). In the EMD-LiNO$_3$ electrolyte, the reduction peaks are combined into one broad peak. The mostly intense

reduction at ∼1.7V appears in the first cycle of the EMD-LiNO$_3$ cell, which disappears on the second cycle, is assigned to the reduction of LiNO$_3$.[48] The relatively high reducibility of LiNO$_3$, before other solvents and salts in the electrolyte, plays important roles in stable SEI formation to facilitate homogeneous transport of Li ions and uniform Li deposition.[48–51]

XPS was used to further understand the effects of the modified carbonate electrolyte on the composition of SEI on the anode. Figure 4D shows that SEI film formed in the LiNO$_3$-containing electrolyte exhibits two peaks at 400.2 eV and 397.1 eV in the N 1s spectra, corresponding to the peaks of LiN$_x$O$_y$ and Li$_3$N, respectively.[52] Li$_3$N possesses superior lithium-ion conductivity and mechanical property, which could improve SEI stability and the cycling performance.[53] The O 1s spectra consist of three peaks (Figure 4E) located at 529.3 eV, 531.9eV, and 532.9 eV, corresponding to inorganic Li$_2$O, organic ROCO$_2$Li, and N–O bond, respectively.[54] In the EMD-LiNO$_3$ electrolyte, the appearance of the N-O bond illustrates the reduction of nitrate, which is consistent with the results in Figures 4D and 4E. Compared with the SEI in EC/EMC, the SEI in EMD-LiNO$_3$ electrolyte possesses increased content of Li$_2$O (45.2% in EC/EMC and 64.7% in EMD-LiNO$_3$) and decreased content of ROCO$_2$Li (54.7% in EC/EMC and 27.3% in EMD-LiNO$_3$). The decreased organic species in the EMD-LiNO$_3$ electrolyte suggests that fewer organic solvents are involved in the anode/electrolyte interfacial reaction. The increased Li$_2$O content show the EMD-LiNO$_3$ electrolyte is able to generate more inorganic components in the SEI, which is also shown in N1s (Figure 4D) and further revealed in the Li 1s spectra (Figure 4F). The Li 1s spectra in the anodes demonstrates three peaks at 52.1, 53.5, and 56.0 eV (Figure 4F), corresponding to Li$_2$O, ROCO$_2$Li, and LiF, respectively.[54] The higher proportion of ROCO$_2$Li in EC/EMC electrolyte show that the reaction between the lithium metal and solvent is more severe than that in EMD-LiNO$_3$ electrolyte. Li$_3$N species show up in the SEI in EMD-LiNO$_3$ cell, which is related to the reduction of nitrate, as mentioned above. Furthermore, the content of LiF species, which is widely known as a stabilizer of the SEI,[55] is also elevated in the EMD-LiNO$_3$ cell. Because of the formation of inorganic-rich SEI in the EMD-LiNO$_3$ cell, the cycle stability of the battery can be effectively enhanced, although the EMD-LiNO$_3$ electrolyte shows similar electrochemical window to the others (Figure S2). Above all, the EMD-LiNO$_3$ electrolyte successfully reduces the side reactions between Li and organic solvents, alleviates electrolyte consumption, and facilitates the formation of more beneficial inorganic components in the SEI, which endow SEI with superior mechanical strength and low ionic transfer barrier, leading to compact and uniform lithium deposition.[56]

Solvation structure and discussion

The solvation structures of different electrolytes are investigated by molecular dynamic (MD) simulation. Figures 5A and 5B show the snapshots of the MD simulated box of the EC/EMC and EMD-LiNO$_3$ electrolytes, and the solvation structure around lithium ions based on the radial distribution functional (RDF) calculation (Figures 5C and 5D). For the EC/EMC electrolyte, EC and EMC solvent molecules are dominant in the first solvation structure. The reasonable coordination number of solvent is 4 as shown in the enlarged figure between Figures 5A and 5B,[57] and the overall ratio of EC and EMC molecules in the solvation shell is 58%/ 42%. In the first solvation shell of Li$^+$ in the EMD-based electrolytes, DMC and EMC molecules dominate in the short-range distance with coordination number of 4, and the overall ratio of DEC and EMC is 59%/41%, and the DEC molecules are in the inner solvation sheath. At the same time, more PF$_6^-$ anions show up in the near neighbor region of the first solvation shell, which may be related to the low dielectric constant of the linear carbonate alkyl. It has been reported that the weakly coordinated solvents are prone to induce PF$_6^-$ anions into the solvated sheath of Li$^+$, improving the anti-reductive stability of the electrolyte and less solvents will be consumed by the side reactions to promote the cycle stability.[36] The PF$_6^-$ anions enter the solvation structure because of the relatively weak solvation between Li$^+$ and linear carbonate alkyl solvents in the EMD-based electrolytes (Figure 5D and S12A), and produce CIP and AGGs structures, as observed in Figures 1B and 1C, which can promote the inorganic components in CEI/SEI and improve the interfacial structural stability,[39] as demonstrated above. The addition of LiNO$_3$ in the EMD electrolyte does not change the solvation structure but reduce the coordination number of DMC and EMC with the appearance of NO$_3^-$ anions in the solvation shell. NO$_3^-$ in the solvation shell would be reduced firstly in the de-solvation process at the anode, as revealed in Figure 4, which can facilitate a stable Li$_3$N/LiN$_x$O$_y$-rich SEI and improve the cycling performance of the batteries.[56]

According to the MSD (Mean Square Displacement) of the lithium ions in the EC/EMC, EMD and EMD-LiNO$_3$ electrolytes (Figures 5E and S12B), the diffusion coefficient in the EMD-LiNO$_3$ and EMD was determined to be 2.5×10^{-7} cm^2 s^{-1} and 2.0×10^{-7} cm^2 s^{-1}, way higher than that (1.4×10^{-7} cm^2 s^{-1})
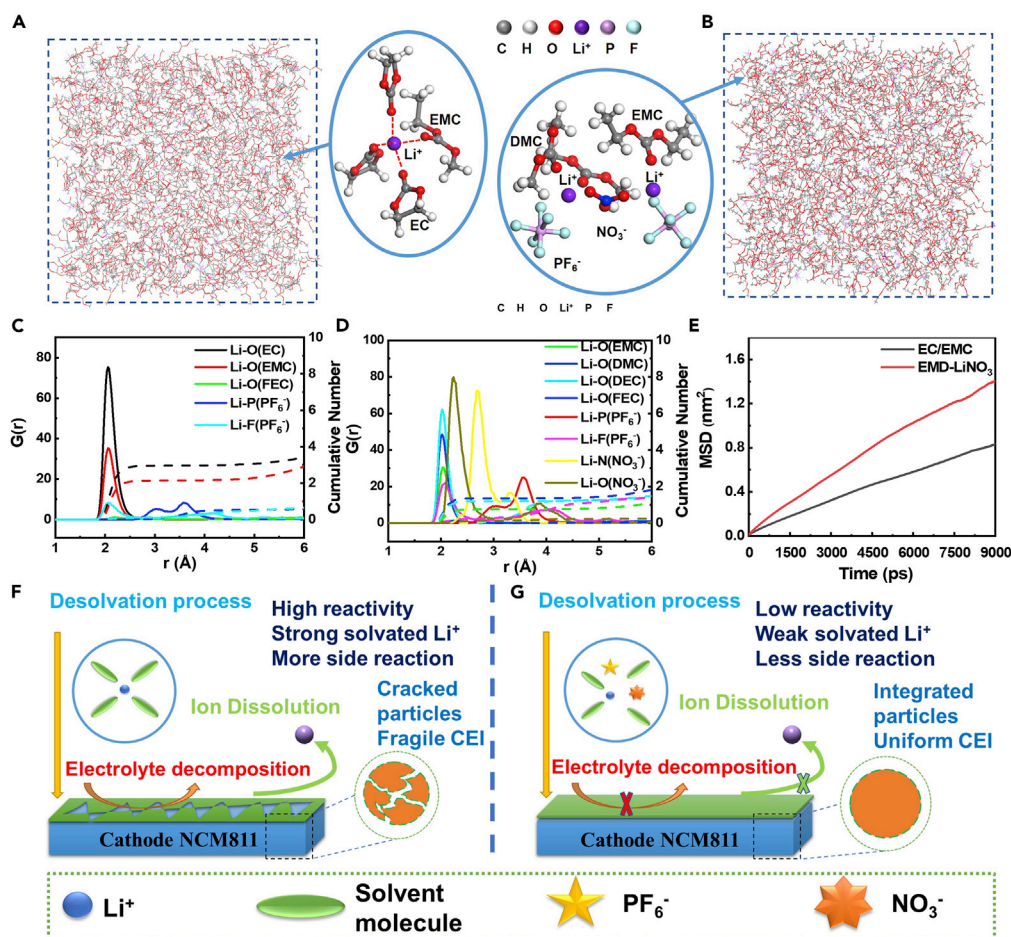
Figure 5. Molecular dynamics simulation and mechanism diagram of electrolytes

(A and B) Snapshots of the MD simulated box of EC/EMC (A) and EMD-LiNO$_3$ (B) electrolytes in ball−stick representation, and corresponding solvation structures of Li ions (insets in the middle).

(C and D) Radial distribution function (g(r), solid line) and cumulative number (dashed line) of lithium ions in EC/EMC (C) and EMD-LiNO$_3$ (D) electrolytes.

(E) Mean square displacement (MSD) of lithium ions in the EC/EMC and EMD-LiNO$_3$ electrolytes.

(F–G) Schematic diagram of the effects of EC/EMC (F) and EMD-LiNO$_3$ (G) electrolytes on the electrolyte-cathode interface.

in the EC/EMC electrolyte. Mean Square Displacement (MSD) is a measure of the deviation of the position of a particle with respect to a reference position over time. It is the most common measure of the spatial extent of random motion following a simple diffusion model.[58] Under this assumption, the diffusion coefficient can be calculated by fitting the slope of the linear part of MSD. However, in actual situation, the diffusion of ions in electrolyte under electric field is more complex. Figure 5E shows the diffusion coefficient obtained by MSD assuming that particles undergo Brownian motion. The EMD system promotes the diffusion of lithium ions in the simple diffusion mode. Besides the diffusion coefficient, the conductivity of the system is also related to the concentration of free lithium ions dissociated per unit volume (Nernst-Einstein equation). The larger dielectric constant of EC enables stronger dissociation ability for lithium ions, leading to higher ionic conductivity (Figure 1E). Therefore, there is no absolute positive correlation between the diffusion coefficient and the conductivity. In addition, the Li$^+$ transference number was measured and calculated according to Figure S13, the EMD-LiNO$_3$ electrolyte possesses the highest transference number of 0.59 among the electrolytes (EMD: 0.42, EC/EMC: 0.48).

The solvation structure and de-solvation process play key roles during the formation of CEI and SEI, which would influence the interfacial stability and cycling performance of the cells. Figures 5F and 5G show the

schematic mechanism of the performance improvement in the EMD-LiNO$_3$ system. As shown above, the EMD-based electrolyte has a relatively weak solvated structure, which allows for the formation of CIPs and AGGs. From an entropic point of view, the addition of DMC molecules contributes to the decrease of the free energy of the cluster.[33] As a result of these fluctuations, the structure around Li$^+$ in the mixed solvents consists of a short-range structure (up to 2 Å from Li$^+$), where the composition is rich in DMC, and by a longer-range structure where the composition is rich in PF$_6^-$. These compositional heterogeneities around a lithium cation are very important for the formation of stable interfacial CEI/SEI layer as well as for the fast lithium-ion transportation kinetics. The weak solvated Li$^+$ by solvent molecules together with the PF$_6^-$ in the solvation structure can effectively reduce side reactions between the electrode and electrolyte during de-solvation process.[36] As a result, compared with the EC/EMC case, stable CEI/SEI layers are formed in EMD-based electrolyte to alleviate continuous consumption of active Li$^+$ and electrolyte. Also, the metal ion dissolution in the cathode can be suppressed and more integrated cathode particles are preserved because of the uniform CEI layer in the EMD-based electrolyte.

As a quantitative criterion of de-solvation, the binding energy between Li$^+$ and electrolyte components is a crucial factor. In addition, the de-solvation barrier would be a key to expand the electrochemical window and facilitate interfacial charge transfer at low temperatures. The Li$^+$ de-solvation barrier is mainly determined by the Li$^+$-solvent complex. The high dielectric constant of EC in EC/EMC electrolyte results in a strong interaction between solvent molecules and Li$^+$, leading to a high de-solvation barrier and a difficult de-solvation process for Li$^+$, especially at low temperatures.[33] By contrast, the de-solvation barrier could be greatly reduced because of the weak solvated Li$^+$ structure in the EMD-based electrolyte. The weak solvated Li$^+$ structure enables fast Li$^+$ de-solvation and transport at the interface between the electrode and electrolyte, leading to reduced interfacial resistance and improved rate performance. Specifically, the outstanding low-temperature cycling performance in the EMD-based electrolyte, as shown in Figure S8, further demonstrate the advantage of the weak solvated structure. Various new solvents have been reported to promote the cycling performance at high voltages and improve the compatibility between electrolyte and NCM/Li metal. However, the high cost and difficulty in synthesis still limits the practical use of these solvents, especially for some fluorine-based solvents.[24–27] The EC-free linear alkyl carbonate electrolyte formulation proposed here provides quite promising perspective to modify the behavior of the electrolyte components for extended cycling performance from the aspects of shifting the coordination structure of Li$^+$ in the solvation shell, accelerating the de-solvation process by weak solvated structure, and optimizing CEI/SEI simultaneously. As a result, the electrochemical performance as well as the low-temperature performance of the battery is greatly enhanced. Moreover, the electrolyte possesses good compatibility with the electrodes and relatively low cost. Despite the progress reported here, more efforts are still needed to explore the EC-free carbonate electrolyte to provide guidelines for advanced electrolytes in the future.

Conclusion

In summary, an EC-free low-cost linear alkyl carbonate-based electrolyte is developed, which enables the high-voltage ($\geq$4.4V) and low-temperature ($-30°C$) application of Ni-rich cathode NCM811. According to the FTIR, Raman, and MD simulation results, the weak solvation between linear ester molecules and lithium ions in the EMD-LiNO$_3$ electrolyte enables the existence of PF$_6^-$ and NO$_3^-$ in the solvation shell, which facilitates stable CEI and SEI on the cathode and anode, respectively. On the other hand, the low reactivity of the linear alkyl carbonate molecules in the solvation structure results in suppressed electrode/electrolyte side reactions and diminished transition metal dissolution at the cathode during cycling. According to the XRD, SEM and electrochemical analysis, it has been confirmed that the EC-free linear alkyl carbonate-based electrolyte can also effectively alleviate the structural changes of Ni-rich cathode materials at high-voltage. The in-situ generated Li$_3$N-LiF-enriched interlayer homogenizes the deposition of Li at the anode. As a result, the Li||NCM811 cell delivers a discharge capacity retention of 93 $\pm$ 0.5% at the voltage of 4.4 V and 88 $\pm$ 0.6% at 4.5V over 100 cycles. In addition, because of the superior low-temperature performance of the electrolyte, the cell delivers remarkable low-temperature capacity and retention, which is twice of the baseline. This study provides very encouraging perspective to develop EC-free carbonate-based electrolyte with wide voltage and temperature windows for high-energy-density lithium batteries.

Limitations of the study

In this work, we developed a weakly solvated EC-free carbonate electrolyte for high-voltage rechargeable lithium batteries. Explorations on the application and adaptability of EC-free carbonate electrolyte in

different cathode/anode materials at different current densities are not thoroughly studied and should be of interest for further studies. Moreover, the feasibility of this concept of electrolyte design and solvation structure manipulation in other battery systems is also worth further investigations.

STAR★METHODS

Detailed methods are provided in the online version of this paper and include the following:

- KEY RESOURCES TABLE
- RESOURCE AVAILABILITY
  - Lead contact
  - Materials availability
  - Data and code availability
- EXPERIMENTAL MODEL AND SUBJECT DETAILS
- METHOD DETAILS
  - Cell assembling
  - Characterizations
  - Electrochemical measurements
  - Theoretical calculations
- QUANTIFICATION AND STATISTICAL ANALYSIS
- ADDITIONAL RESOURCES

SUPPLEMENTAL INFORMATION

Supplemental information can be found online at https://doi.org/10.1016/j.isci.2022.105710.

AUTHOR CONTRIBUTIONS

G.K.: Investigation, conceptualization, methodology, data curation, validation, writing – original draft preparation; G.Z. and X.R.: Formal analysis; J.M.: Molecular dynamics simulation; R.Y., K.C., and T.J.: Investigation; K.Y., P.Q., Z.C., and F.K.: Supervision, writing – reviewing and editing; Y.C.: Supervision, investigation, conceptualization, methodology, data curation, validation, funding acquisition, project administration and writing – reviewing and editing.

DECLARATION OF INTERESTS

The authors declare no conflict of interest.

INCLUSION AND DIVERSITY

We support inclusive, diverse, and equitable conduct of research.

REFERENCES

1. Li, S., Zhao, D., Wang, P., Cui, X., and Tang, F. (2016). Electrochemical effect and mechanism of adiponitrile additive for high-voltage electrolyte. Electrochim. Acta *222*, 668–677. https://doi.org/10.1016/j.electacta.2016.11.022.

2. Ren, X., Zou, L., Cao, X., Engelhard, M.H., Liu, W., Burton, S.D., Lee, H., Niu, C., Matthews, B.E., Zhu, Z., et al. (2019). Enabling high-voltage lithium-metal batteries under practical conditions. Joule *3*, 1662–1676. https://doi.org/10.1016/j.joule.2019.05.006.

3. Jie, Y., Liu, X., Lei, Z., Wang, S., Chen, Y., Huang, F., Cao, R., Zhang, G., and Jiao, S. (2020). Enabling high-voltage lithium metal batteries by manipulating solvation structure in ester electrolyte. Angew. Chem. Int. Ed. Engl. *59*, 3505–3510. https://doi.org/10.1002/anie.201914250.

4. Zhang, C., Niu, Z., Ding, Y., Zhang, L., Zhou, Y., Guo, X., Zhang, X., Zhao, Y., and Yu, G. (2018). Highly concentrated phthalimide-based anolytes for organic redox flow batteries with enhanced reversibility. Chem *4*,

2814–2825. https://doi.org/10.1016/j.chempr.2018.08.024.

5. Dong, Q., Yao, X., Zhao, Y., Qi, M., Zhang, X., Sun, H., He, Y., and Wang, D. (2018). Cathodically stable Li-O$_2$ battery operations using water-in-salt electrolyte. Chem 4, 1345–1358. https://doi.org/10.1016/j.chempr.2018.02.015.

6. Zhong, Q., Bonakdarpour, A., Zhang, M., Gao, Y., and Dahn, J.R. (1997). Synthesis and electrochemistry of LiNi$_x$Mn$_{2-x}$O$_4$. J. Electrochem. Soc. 144, 205–213. https://doi.org/10.1149/1.1837386.

7. Amine, K. (1999). Olivine LiCoPO$_4$ as 4.8 V electrode material for lithium batteries. Electrochem. Solid State Lett. 3, 178. https://doi.org/10.1149/1.1390994.

8. Liu, Q., Yang, G., Li, S., Zhang, S., Chen, R., Wang, Z., and Chen, L. (2021). Synergy effect of trimethyl borate on protecting high-voltage cathode materials in dual-additive electrolytes. ACS Appl. Mater. Interfaces 13, 21459–21466. https://doi.org/10.1021/acsami.1c04389.

9. Wu, F., Tian, J., Su, Y., Wang, J., Zhang, C., Bao, L., He, T., Li, J., and Chen, S. (2015). Effect of Ni(2+) content on lithium/nickel disorder for Ni-rich cathode materials. ACS Appl. Mater. Interfaces 7, 7702–7708. https://doi.org/10.1021/acsami.5b00645.

10. Borodin, O. (2019). Challenges with prediction of battery electrolyte electrochemical stability window and guiding the electrode – electrolyte stabilization. Current Opinion in Electrochemistry 13, 86–93. https://doi.org/10.1016/j.coelec.2018.10.015.

11. Lan, G., Zhou, H., Xing, L., Chen, J., Li, Z., Guo, R., Che, Y., and Li, W. (2019). Insight into the interaction between Ni-rich LiNi0.8Co0.1Mn0.1O2 cathode and BF4$^-$–introducing electrolyte at 4.5 V high voltage. J. Energy Chem. 39, 235–243. https://doi.org/10.1016/j.jechem.2019.04.011.

12. Tsai, Y.-C., Kuo, C.-T., Liu, S.-F., Lee, Y.-T., and Yew, T.-R. (2021). Effect of different electrolytes on MnO2 anodes in lithium-ion batteries. J. Phys. Chem. C 125, 1221–1233. https://doi.org/10.1021/acs.jpcc.0c09022.

13. Zhang, S.S. (2020). Understanding of performance degradation of LiNi$_{0.8}$Co$_{0.1}$Mn$_{0.1}$O$_2$ cathode material operating at high potentials. J. Energy Chem. 41, 135–141. https://doi.org/10.1016/j.jechem.2019.05.013.

14. Han, S., Liu, Y., Zhang, H., Fan, C., Fan, W., Yu, L., and Du, X. (2019). Succinonitrile as a high-voltage additive in the electrolyte of LiNi$_{0.5}$Co$_{0.2}$Mn$_{0.3}$O$_2$/graphite full batteries. Surf. Interface Anal. 52, 364–373. https://doi.org/10.1002/sia.6744.

15. Duan, K., Ning, J., Zhou, L., Wang, S., Wang, Q., Liu, J., and Guo, Z. (2022). Synergistic inorganic-organic dual-additive electrolytes enable practical high-voltage lithium-ion batteries. ACS Appl. Mater. Interfaces 14,

16. Xia, J., Liu, Q., Hebert, A., Hynes, T., Petibon, R., and Dahn, J.R. (2017). Succinic anhydride as an enabler in ethylene carbonate-free linear alkyl carbonate electrolytes for high voltage Li-ion cells. J. Electrochem. Soc. 164, A1268–A1273. https://doi.org/10.1149/2.1341706jes.

17. Xia, J., Glazier, S.L., Petibon, R., and Dahn, J.R. (2017). Improving linear alkyl carbonate electrolytes with electrolyte additives. J. Electrochem. Soc. 164, A1239–A1250. https://doi.org/10.1149/2.1321706jes.

18. Cheng, H., Sun, Q., Li, L., Zou, Y., Wang, Y., Cai, T., Zhao, F., Liu, G., Ma, Z., Wahyudi, W., et al. (2022). Emerging Era of electrolyte solvation structure and interfacial model in batteries. ACS Energy Lett. 7, 490–513. https://doi.org/10.1021/acsenergylett.1c02425.

19. Zou, Y., Cao, Z., Zhang, J., Wahyudi, W., Wu, Y., Liu, G., Li, Q., Cheng, H., Zhang, D., Park, G.T., et al. (2021). Interfacial model deciphering high-voltage electrolytes for high energy density, high safety, and fast-charging lithium-ion batteries. Adv. Mater. 33, e2102964. https://doi.org/10.1002/adma.202102964.

20. Zhang, T., and Paillard, E. (2018). Recent advances toward high voltage, EC-free electrolytes for graphite-based Li-ion battery. Front. Chem. Sci. Eng. 12, 577–591. https://doi.org/10.1007/s11705-018-1758-z.

21. Abu-Lebdeh, Y., and Davidson, I. (2009). High-voltage electrolytes based on adiponitrile for Li-ion batteries. J. Electrochem. Soc. 156, A60. https://doi.org/10.1149/1.3023084.

22. Abouimrane, A., Belharouak, I., and Amine, K. (2009). Sulfone-based electrolytes for high-voltage Li-ion batteries. Electrochem. Commun. 11, 1073–1076. https://doi.org/10.1016/j.elecom.2009.03.020.

23. Zhang, Z., Hu, L., Wu, H., Weng, W., Koh, M., Redfern, P.C., Curtiss, L.A., and Amine, K. (2013). Fluorinated electrolytes for 5 V lithium-ion battery chemistry. Energy Environ. Sci. 6, 1806. https://doi.org/10.1039/C3EE24414H.

24. Xue, W., Shi, Z., Huang, M., Feng, S., Wang, C., Wang, F., Lopez, J., Qiao, B., Xu, G., Zhang, W., et al. (2020). FSI-inspired solvent and "full fluorosulfonyl" electrolyte for 4 V class lithium-metal batteries. Energy Environ. Sci. 13, 212–220. https://doi.org/10.1039/C9EE02538C.

25. Xue, W., Huang, M., Li, Y., Zhu, Y.G., Gao, R., Xiao, X., Zhang, W., Li, S., Xu, G., Yu, Y., et al. (2021). Ultra-high-voltage Ni-rich layered cathodes in practical Li metal batteries enabled by a sulfonamide-based electrolyte. Nat. Energy 6, 495–505. https://doi.org/10.1038/s41560-021-00792-y.

26. Yu, Z., Wang, H., Kong, X., Huang, W., Tsao, Y., Mackanic, D.G., Wang, K., Wang, X., Huang, W., Choudhury, S., et al. (2020). Molecular design for electrolyte solvents enabling energy-dense and long-cycling

lithium metal batteries. Nat. Energy 5, 526–533. https://doi.org/10.1038/s41560-020-0634-5.

27. Yu, Z., Rudnicki, P.E., Zhang, Z., Huang, Z., Celik, H., Oyakhire, S.T., Chen, Y., Kong, X., Kim, S.C., Xiao, X., et al. (2022). Rational solvent molecule tuning for high-performance lithium metal battery electrolytes. Nat. Energy 7, 94–106. https://doi.org/10.1038/s41560-021-00962-y.

28. Li, Q., Liu, G., Cheng, H., Sun, Q., Zhang, J., and Ming, J. (2021). Low-temperature electrolyte design for lithium-ion batteries: prospect and challenges. Chemistry 27, 15842–15865. https://doi.org/10.1002/chem.202101407.

29. Lim, J., Lee, K.-K., Liang, C., Park, K.-H., Kim, M., Kwak, K., and Cho, M. (2019). Two-dimensional infrared spectroscopy and molecular dynamics simulation studies of nonaqueous lithium ion battery electrolytes. J. Phys. Chem. B 123, 6651–6663. https://doi.org/10.1021/acs.jpcb.9b02026.

30. Chapman, N., Borodin, O., Yoon, T., Nguyen, C.C., and Lucht, B.L. (2017). Spectroscopic and density functional theory characterization of common lithium salt solvates in carbonate electrolytes for lithium batteries. J. Phys. Chem. C 121, 2135–2148. https://doi.org/10.1021/acs.jpcc.6b12234.

31. Bogle, X., Vazquez, R., Greenbaum, S., Cresce, A.v.W., and Xu, K. (2013). Understanding Li+–Solvent interaction in nonaqueous carbonate electrolytes with 17O NMR. J. Phys. Chem. Lett. 4, 1664–1668. https://doi.org/10.1021/jz400661k.

32. Pyun, S.-I., and Ryu, Y.-G. (1998). In-situ spectroelectrochemical analysis of the passivating surface film formed on a graphite electrode during the electrochemical reduction of lithium salts and organic carbonate solvent. J. Electroanal. Chem. 455, 11–17. https://doi.org/10.1016/S0022-0728(98)00154-5.

33. Wang, Z., Wang, H., Qi, S., Wu, D., Huang, J., Li, X., Wang, C., and Ma, J. (2022). Structural regulation chemistry of lithium ion solvation for lithium batteries. EcoMat 4. https://doi.org/10.1002/eom2.12200.

34. Suo, L., Borodin, O., Gao, T., Olguin, M., Ho, J., Fan, X., Luo, C., Wang, C., and Xu, K. (2015). "Water-in-salt" electrolyte enables high-voltage aqueous lithium-ion chemistries. Science 350, 938–943. https://doi.org/10.1126/science.aab1595.

35. Malik, R.A., Lone, M.R., Ahmed, A., Koul, K.A., and Malla, R.R. (2017). Aqueous Li-ion batteries: now in striking distance. Joule 1, 17–19. https://doi.org/10.1016/j.joule.2017.08.016.

36. Liu, X., Shen, X., Li, H., Li, P., Luo, L., Fan, H., Feng, X., Chen, W., Ai, X., Yang, H., and Cao, Y. (2021). Ethylene carbonate-free propylene carbonate-based electrolytes with excellent electrochemical compatibility for Li-ion batteries through engineering electrolyte solvation structure. Adv. Energy Mater. 11, 2003905. https://doi.org/10.1002/aenm.202003905.

37. Ming, J., Cao, Z., Li, Q., Wahyudi, W., Wang, W., Cavallo, L., Park, K.-J., Sun, Y.-K., and Alshareef, H.N. (2019). Molecular-scale interfacial model for predicting electrode performance in rechargeable batteries. ACS Energy Lett. *4*, 1584–1593. https://doi.org/10.1021/acsenergylett.9b00822.

38. Miele, E., Dose, W.M., Manyakin, I., Frosz, M.H., Ruff, Z., De Volder, M.F.L., Grey, C.P., Baumberg, J.J., and Euser, T.G. (2022). Hollow-core optical fibre sensors for operando Raman spectroscopy investigation of Li-ion battery liquid electrolytes. Nat. Commun. *13*, 1651. https://doi.org/10.1038/s41467-022-29330-4.

39. Su, L., Jo, E., and Manthiram, A. (2022). Protection of cobalt-free LiNiO2 from degradation with localized saturated electrolytes in lithium-metal batteries. ACS Energy Lett. *7*, 2165–2172. https://doi.org/10.1021/acsenergylett.2c01081.

40. Lv, Y., Huang, S., Lu, S., Ding, W., Yu, X., Liang, G., Zou, J., Kang, F., Zhang, J., and Cao, Y. (2022). B_2O_3/$LiBO_2$ dual-modification layer stabilized Ni-rich cathode for lithium-ion battery. J. Power Sources *536*, 231510. https://doi.org/10.1016/j.jpowsour.2022.231510.

41. Kasnatscheew, J., Evertz, M., Streipert, B., Wagner, R., Nowak, S., Cekic Laskovic, I., and Winter, M. (2017). Changing established belief on capacity fade mechanisms: thorough investigation of $LiNi_{1/3}Co_{1/3}Mn_{1/3}O_2$ (NCM111) under high voltage conditions. J. Phys. Chem. C *121*, 1521–1529. https://doi.org/10.1021/acs.jpcc.6b11746.

42. Zhang, X., Zou, L., Xu, Y., Cao, X., Engelhard, M.H., Matthews, B.E., et al. (2020). Advanced electrolytes for fast-charging high-voltage lithium-ion batteries in wide-temperature range. Adv. Energy Mater. *10*, 2000368. https://doi.org/10.1002/aenm.202000368.

43. Zhou, C.-x., Wang, P.-b., Zhang, B., Tang, L.-b., Tong, H., He, Z.-j., and Zheng, J.-c. (2019). Formation and effect of residual lithium compounds on Li-rich cathode material $Li_{1.35}[N_{i0.35}Mn_{0.65}]O_2$. ACS Appl. Mater. Interfaces *11*, 11518–11526. https://doi.org/10.1021/acsami.9b01806.

44. Qu, X., Huang, H., Wan, T., Hu, L., Yu, Z., Liu, Y., Dou, A., Zhou, Y., Su, M., Peng, X., et al. (2022). An integrated surface coating strategy to enhance the electrochemical performance of nickel-rich layered cathodes. Nano Energy *91*, 106665. https://doi.org/10.1016/j.nanoen.2021.106665.

45. Li, T., Li, X., Wang, Z., and Guo, H. (2017). A short process for the efficient utilization of transition-metal chlorides in lithium-ion batteries: a case of $LiNi_{0.8}Co_{0.1}Mn_{0.1}O_2$ and $LiNi_{0.8}Co_{0.1}Mn_{0.1}O_2$. J. Power Sources *342*, 495–503. https://doi.org/10.1016/j.jpowsour.2016.12.095.

46. Li, X., Zhang, K., Wang, M., Liu, Y., Qu, M., Zhao, W., and Zheng, J. (2018). Dual functions of zirconium modification on improving the electrochemical performance of Ni-rich $LiNi_{0.8}Co_{0.1}Mn_{0.1}O_2$. Sustain. Energy Fuels *2*, 413–421. https://doi.org/10.1039/C7SE00513J.

47. Zhao, W., Zheng, J., Zou, L., Jia, H., Liu, B., Wang, H., Engelhard, M.H., Wang, C., Xu, W., Yang, Y., and Zhang, J. (2018). High voltage operation of Ni-rich NMC cathodes enabled by stable electrode/electrolyte interphases. Adv. Energy Mater. *8*, 1800297. https://doi.org/10.1002/aenm.201800297.

48. Liu, Y., Lin, D., Li, Y., Chen, G., Pei, A., Nix, O., Li, Y., and Cui, Y. (2018). Solubility-mediated sustained release enabling nitrate additive in carbonate electrolytes for stable lithium metal anode. Nat. Commun. *9*, 3656. https://doi.org/10.1038/s41467-018-06077-5.

49. Zhang, X.-Q., Li, T., Li, B.-Q., Zhang, R., Shi, P., Yan, C., Huang, J.-Q., and Zhang, Q. (2020). A sustainable solid electrolyte interphase for high-energy-density lithium metal batteries under practical conditions. Angew. Chem. Int. Ed. Engl. *59*, 3252–3257. https://doi.org/10.1002/anie.201911724.

50. Piao, N., Liu, S., Zhang, B., Ji, X., Fan, X., Wang, L., Wang, P.-F., Jin, T., Liou, S.-C., Yang, H., et al. (2021). Lithium metal batteries enabled by synergetic additives in commercial carbonate electrolytes. ACS Energy Lett. *6*, 1839–1848. https://doi.org/10.1021/acsenergylett.1c00365.

51. Zhang, S.S. (2012). Effect of discharge cutoff voltage on reversibility of lithium/sulfur batteries with $LiNO_3^-$contained electrolyte. J. Electrochem. Soc. *159*, A920–A923. https://doi.org/10.1149/2.002207jes.

52. Zhang, X.-Q., Chen, X., Cheng, X.-B., Li, B.-Q., Shen, X., Yan, C., Huang, J.-Q., and Zhang, Q. (2018). Highly stable lithium metal batteries enabled by regulating the solvation of lithium ions in nonaqueous electrolytes. Angew. Chem. Int. Ed. Engl. *57*, 5301–5305. https://doi.org/10.1002/anie.201801513.

53. Ren, X., Chen, S., Lee, H., Mei, D., Engelhard, M.H., Burton, S.D., Zhao, W., Zheng, J., Li, Q., Ding, M.S., et al. (2018). Localized high-concentration sulfone electrolytes for high-efficiency lithium-metal batteries. Chem *4*, 1877–1892. https://doi.org/10.1016/j.chempr.2018.05.002.

54. Yan, C., Yao, Y.-X., Chen, X., Cheng, X.-B., Zhang, X.-Q., Huang, J.-Q., and Zhang, Q. (2018). Lithium nitrate solvation chemistry in carbonate electrolyte sustains high-voltage lithium metal batteries. Angew. Chem. Int. Ed. Engl. *57*, 14055–14059. https://doi.org/10.1002/anie.201807034.

55. Huang, W., Wang, H., Boyle, D.T., Li, Y., and Cui, Y. (2020). Resolving nanoscopic and mesoscopic heterogeneity of fluorinated species in battery solid-electrolyte interphases by cryogenic electron microscopy. ACS Energy Lett. *5*, 1128–1135. https://doi.org/10.1021/acsenergylett.0c00194.

56. Xiao, P., Luo, R., Piao, Z., Li, C., Wang, J., Yu, K., Zhou, G., and Cheng, H.-M. (2021). High-performance lithium metal batteries with a wide operating temperature range in carbonate electrolyte by manipulating interfacial chemistry. ACS Energy Lett. *6*, 3170–3179. https://doi.org/10.1021/acsenergylett.1c01528.

57. Zheng, T., Xiong, J., Shi, X., Zhu, B., Cheng, Y.-J., Zhao, H., and Xia, Y. (2021). Cocktail therapy towards high temperature/high voltage lithium metal battery via solvation sheath structure tuning. Energy Storage Mater. *38*, 599–608. https://doi.org/10.1016/j.ensm.2021.04.002.

58. Kusumi, A., Sako, Y., and Yamamoto, M. (1993). Confined lateral diffusion of membrane receptors as studied by single particle tracking (nanovid microscopy). Effects of calcium-induced differentiation in cultured epithelial cells. Biophys. J. *65*, 2021–2040. https://doi.org/10.1016/S0006-3495(93)81253-0.

STAR★METHODS

KEY RESOURCES TABLE

REAGENT or RESOURCE	SOURCE	IDENTIFIER
Others		
Li foil	Guangdong Canrd New Energy Technology Co.,Ltd.	7439-93-2
Graphite	Guangdong Canrd New Energy Technology Co.,Ltd.	7782-42-5
LiNi0.8Co0.1Mn0.1O2	Guangdong Canrd New Energy Technology Co.,Ltd.	http://www.canrd.com/index
Ethylene carbonate	Dodo Chem Co., Ltd.	96-49-1
Ethyl Methyl Carbonate	Dodo Chem Co., Ltd.	623-53-0
Dimethyl carbonate	Dodo Chem Co., Ltd.	616-38-6
Diethyl carbonate	Dodo Chem Co., Ltd.	105-58-8
Fluoroethylene carbonate	Dodo Chem Co., Ltd.	114435-02-8
Lithium Hexafluorophosphate	Dodo Chem Co., Ltd.	21324-40-3

RESOURCE AVAILABILITY

Lead contact

Further information and requests for resources and reagents should be directed to and will be fulfilled by the lead contact Yidan Cao (yidancao@sz.tsinghua.edu.cn).

Materials availability

This study did not generate new unique reagents.

Data and code availability

- All data reported in this paper will be shared by the lead contact upon request.

- This paper does not report original code.

- Any additional information required to reanalyze the data reported in this paper is available from the lead contact upon request.

EXPERIMENTAL MODEL AND SUBJECT DETAILS

Battery grade EC, EMC, DMC, DEC, FEC, and $LiPF_6$ $LiNO_3$ were purchased from Suzhou Dodo Chemical Technology Co. Ltd (China) and used as received. 1.0 M $LiPF_6$ EC/EMC (3:7, Vol.%)+ 2 vol.% FEC (denoted by EC/EMC), 1.0 M $LiPF_6$ EC/EMC (3:7, Vol.%) +2 vol.% FEC with 1 wt% $LiNO_3$ additive (denoted by EMC-$LiNO_3$), 1.0 M $LiPF_6$ EMC/DMC/DEC (1:1:1, Vol.%) +2 vol.% FEC with 1 wt% $LiNO_3$ additive (denoted by EMD-$LiNO_3$), 1.0 M $LiPF_6$ EMC/DMC/DEC (1:1:1, Vol.%) +2 vol.% FEC (denoted by EMD) and 1.0 M $LiPF_6$ EMC/DMC/DEC (1:1:1, Vol.%) +2 vol.% FEC with 1 wt% $LiNO_3$ additive (denoted by EMD-$LiNO_3$) were prepared in argon filled box with oxygen and water content below 0.1 ppm.Additionally, 1.0 M $LiPF_6$ EC/DMC/DEC (1:1:1, Vol.%) +2 vol.% FEC, 1.0 M $LiPF_6$ EC/EMC/DEC (1:1:1, Vol.%) +2 vol.% FEC, 1.0 M $LiPF_6$ EMC/DMC/DEC (2:1:1, Vol.%) +2 vol.% FEC (denoted by EMD2) and 1.0 M $LiPF_6$ EMC/DMC/DEC (4:1:1, Vol.%) +2 vol.% FEC (denoted by EMD4) were prepared in argon filled box with oxygen and water content below 0.1 ppm.

Li metal chips (φ = 1.55 cm, thickness = 450 μm) were purchased from Guangdong Canrd New Energy Technology Co. Ltd. The Ni-rich cathode was prepared by coating slurry of 80 wt.% $LiNi_{0.8}Co_{0.1}Mn_{0.1}O_2$ (NCM811, Guangdong Canrd New Energy Technology Co. Ltd), 10 wt% super-P (Guangdong Canrd New Energy Technology Co. Ltd) and 10 wt.% PVDF binder (Guangdong Canrd New Energy Technology Co. Ltd) uniformly on the Al foil (Loading: 4.5 $\pm$ 0.5 mg cm^{-2}). Graphite electrode was prepared by coating slurry of 80 wt.% graphite (Guangdong Canrd New Energy Technology Co. Ltd), 10 wt.% super-P and 10 wt.% PVDF binder were coated uniformly on the Cu foil (Loading: 2.5 $\pm$ 0.5 mg cm^{-2}).

METHOD DETAILS

Cell assembling

CR2032 and CR2025 coin-cell kits were purchased from Guangdong Canrd New Energy Technology Co. Ltd. Coin cells were assembled inside an argon-fill glove box (MIKROUNA, H_2O < 0.1 ppm, O_2< 0.1 ppm). For Li||Cu CR2032 cells, a Li chip, a piece of polyethylene (PE) separator (φ = 1.6 cm), and a piece of Cu foil (φ = 1.2cm) were stacked together. For Li||NCM811 CR2032 cells, the Li chip, PE separator, and punched disk of NCM811 cathode were assembled. For Graphite||NCM811 (N/P = 1.1) CR2025 full cell, the punched disk of graphite anode (φ = 1.2 cm), NCM cathode (φ = 1.2 cm) and PE separator were used. 75 μL of electrolyte was added in the coin cell if not specified.

Characterizations

The conductivity of the electrolyte was measured by a DDB-11A conductivity meter (Hangzhou Qiwei, China) in the temperature range of −15 to 30°C. The viscosity of the electrolyte was measured with an Anton Paar rheometer MCR302 (Shanghai, China). The temperature of samples was initially set at 5°C to start the measurements. Once a measurement was started, temperature was increased linearly from 15 to 45°C in a time interval of 7 min while the viscosity was measured and recorded, with a shear rate of 90 1/s.

Infrared spectrometer (PerkinElmer Frontier, Waltham, Massachusetts, USA) and Raman spectrometer (Horiba LabRAM HR800) were used to identify the structure of the electrolytes. In order to obtain ex-situ results of cycled cells, the coin cells were disassembled in the argon-filled glove box. The cycled electrodes were washed by high purity anhydrous DMC for three times to remove $LiPF_6$ salt and the solvents residues. After dried in the glove box for 12 h, surface morphology of the electrodes was characterized.

The crystalline structure of the samples was characterized by X-ray diffractometer (XRD Bruker D8 Advance) with Cu-Kα radiation (λ = 1.5406 Å) in the 2θ range of 10°-80° at a step rate of 10° min^{-1}. Surface morphology of the cathodes and anodes were characterized under a field-emission scanning electron microscope (SEM, 5 Kv, HITACHI SU8010, 20~2000 times (low magnification mode), 100~800000 times (high magnification mode). The surface chemistry of the samples were characterized by X-ray photoelectron spectroscopy (XPS) on a PHI 5000 VersaProbe II equipment with Al radiation source. The binding energy was calibrated internally by the C 1s binding energy (B.E.) of 284.8 eV. After subtraction of a Shirley-type background, XPS spectra were fitted by Gaussian-Lorentzian functions. The chemical compositions, binding energies and full width at half maximum of all spectra are provided in supporting information Tables S2 and S3.

Electrochemical measurements

Galvanostatic cycling tests were conducted within a voltage window of 2.8–4.4 (4.5) V (Li||NCM811) or 2.7–4.3 V (Graphite||NCM811) using Land battery testers (Wuhan Land, China) at 25°C. After one formation cycle at C/10 rates (1C = 170 mAh g^{-1}), the Li||NCM811 cells were charged to 4.4 V or 4.5 Vat 1C and held at 4.4 (4.5) V until the anodic current dropped below C/20 before discharged to 2.8 V at 1C, followed by a rest step of 5 min for each charge/discharge process. Li||NCM811 cells were tested at various currents to obtain the rate performance. For Li||Cu cells, fixed amounts of Li (areal capacity of 1.0 mAh cm^{-2}) was deposited onto the bare Cu substrate at current density of 1 mA cm^{-2} after two formation cycles, and then fully stripped until a cutoff voltage of 1 V in each cycle. LSV and cyclic voltammetry (CV) were carried out at a scan rate of 1 and 0.1 mV s^{-1}, respectively. The EIS was tested in a frequency range from 10 MHz to 0.01 Hz with an AC signal amplitude of 10 mV. LSV, CV, and EIS data were collected on the Biologic electrochemical workstation (France).

Theoretical calculations

MD simulation was performed using Gromacs (2019.5 version, http://www.gromacs.org). For EC-based electrolyte, 358 EC, 540 EMC, 22 FEC and 80 $LiPF_6$ molecules were added to an 8 × 8 × 8 nm simulation box, in accordance with the experimental density and stoichiometry. For the EMD electrolyte, 288 EMC, 246 DEC, 352 DMC, 24 FEC and 89 $LiPF_6$ molecules were added to the 8 × 8 × 8 nm simulation box. For the EMD-$LiNO_3$ electrolyte, 284 EMC, 243 DEC, 348 DMC, 24 FEC, 88 $LiPF_6$ and 12 $LiNO_3$ molecules were added to the 8 × 8 × 8 nm simulation box. OPLS-AA force field was adopted in this study to describe the inter- and intra-molecular interactions. The parameters for solvent molecules (DEC, EC, EMC, DMC, FEC) were generated automatically using the LigParGen Server. All force field parameters were provided

in.itp files and nonbonding parameters for solvent molecules. All simulations started with a 2 ns NPT run at 500 K, followed by a 3 ns NPT annealing process, in which the system temperature dropped from 330 K to room temperature (298 K). In this way, a homogeneous single-phase solution was prepared as the initial configuration. Then, the system was equilibrated with a 5 ns NPT and a 10 ns NVT simulation, before a 5 ns production run for RDF and MSD calculation. Nose-Hoover thermostat and Berendsen barostat were used to control the temperature and the pressure, respectively, and in all simulations the time step was set to be 1.0 fs. All the snapshots of MD trajectories were visualized via VMD (https://www.ks.uiuc.edu/Research/vmd/).

QUANTIFICATION AND STATISTICAL ANALYSIS

The loading weight of the active materials in the electrode is calculted by the equation: Loading = $(M_e - M_{Al})$ *w. Where M_e and M_{Al} are respectively the mass of the electrode and the current collector, w is the weight percent of the active material in the electrode. The errors in the loading come from the weight measurement.

ADDITIONAL RESOURCES

There is no relevant resource.